Communications Materials

https://doi.org/10.1038/s43246-026-01213-x

Article in Press

Demonstration of overcoming 20% efficiency in kesterite/perovskite tandem solar cells on rigid and flexible substrates

Received: 20 October 2025

Accepted: 22 May 2026

Cite this article as: Gobbo, C., Trifiletti, V., Tseberlidis, G. *et al.* Demonstration of overcoming 20% efficiency in kesterite/perovskite tandem solar cells on rigid and flexible substrates. *Commun Mater* (2026). https://doi.org/10.1038/s43246-026-01213-x

Carla Gobbo, Vanira Trifiletti, Giorgio Tseberlidis, Yuancai Gong, Alex Jimenez-Arguijo, Chiara Boldrini, Jessica Barichello, Luigi Angelo Castriotta, Yassine Raoui, Paolo Mariani, Fabio Matteocci, Aldo Di Carlo, Paolo Biagini, Edgardo Saucedo, Riccardo Po & Simona Binetti

Demonstration of Overcoming 20% Efficiency in Kesterite/Perovskite Tandem Solar Cells on Rigid and Flexible Substrates

Carla Gobbo[a,b]*, Vanira Trifiletti[a], Giorgio Tseberlidis[a,c], Yuancai Gong[d,e], Alex Jimenez-Arguijo[d,e], Chiara Boldrini[a], Jessica Barichello[f], Luigi Angelo Castriotta[g], Yassine Raoui[g,h], Paolo Mariani[f], Fabio Matteocci[g], Aldo Di Carlo[f,g], Paolo Biagini[b], Edgardo Saucedo[d,e]*, Riccardo Po[b], Simona Binetti[a]

[a] *Department of Materials Science and Solar Energy Research Center (MIB-SOLAR), University of Milano-Bicocca, Via Cozzi 55, 20125, Milan (Italy)*

[b] *ENI S.p.A. – New Energies, Renewable Energies and Materials Science Research Center, 28100 Novara (Italy).*

[c] *CNR-ISSMC Istituto di Scienza, Tecnologia e Sostenibilità per lo sviluppo dei Materiali Ceramici, Via Granarolo 64, 48018, Faenza (RA), Italy*

[d] *Photovoltaic group, Electronic Engineering department, Polytechnic University of Catalonia (UPC), Av. Eduard Maristany, 16, 08019, Barcelona (Spain)*

[e] *Universitat Politècnica de Catalunya (UPC), Barcelona Centre for Multiscale Science & Engineering, Av Eduard Maristany 10-14, 08019, Barcelona (Spain)*

[f] *CNR - Istituto di Struttura della Materia, Area di Ricerca di Tor Vergata, Via Fosso del Cavaliere 100, 00133, Rome (Italy)*

[g] *CHOSE – Centre for Hybrid and Organic Solar Energy, Department of Electronic Engineering, University of Rome ''Tor Vergata'', via del Politecnico 1, Roma 00133, Italy*

[h] *IPVF, Institut Photovoltaïque d'Ile-de-France (IPVF), 18 boulevard Thomas Gobert, 91120 Palaiseau, France*

Corresponding authors: Carla Gobbo, Edgardo Saucedo
Email corresponding authors:c.gobbo3@campus.unimib.it, edgardo.saucedo@upc.edu

Abstract

Among emerging thin-film solar cells, kesterite $Cu_2ZnSn(S,Se)_4$ (CZTSSe) absorbers offer several advantages: they are based on earth-abundant, non-toxic elements and combine high stability, tunable bandgap (E_g), and flexibility, key features for integrated photovoltaic (PV) applications. Selenium-rich CZTSSe (E_g of 1.1 eV) is an ideal bottom-cell candidate for flexible tandem devices with perovskites, thereby maximising efficiency. However, CZTSSe/perovskite tandems are still

underexplored. Here, we report an effective solution-based route for producing high-efficiency CZTSSe bottom cells on both rigid Mo-coated soda-lime-glass and flexible Mo-foil substrates. To optimise absorber morphology and grain size, Na-doping and Ag-alloying were performed. Then, 4-Terminal (4T) tandem devices combining kesterite- and perovskite-based subcells were designed. Solution-processed $Cs_{0.17}FA_{0.83}Pb(I_{0.90}Br_{0.10})_3$ perovskites (E_g of 1.63 eV) ensured optimal bandgap matching and broadened light harvesting, yielding efficiencies exceeding 22% and 20% for rigid and flexible 4T tandem devices, respectively. This proof-of-concept solution-processed tandem approach represents a promising step toward developing cost-effective and sustainable PV technologies, with promising results for future solar energy applications.

Introduction

The lightweight and mechanically flexible thin-film photovoltaic (PV) technologies hold significant potential for next-generation application scenarios, including Product Integrated Photovoltaics (PIPV), Building Integrated Photovoltaics (BIPV), Vehicle Integrated Photovoltaics (VIPV), as well as indoor and wearable devices [1–3]. Thanks to their conformability and bendability, these solar cells can be easily adapted to infrastructures with various shapes, curvatures, and sizes, while offering a faster payback compared to traditional rigid and heavy PV systems [4]. In this field, tandem architectures based on intrinsically flexible thin-film absorbers are therefore particularly attractive, as they provide a pathway to simultaneously achieve high efficiency, low weight, and mechanical conformability. However, identifying a material that is intrinsically flexible and fully compatible with low-cost manufacturing remains a critical challenge. Kesterite inorganic materials represent an attractive solution, offering several advantages. Above all, they are low-cost and environmentally friendly p-type semiconductors, and they exhibit high stability, direct and tuneable bandgap (E_g), and high absorption coefficient ($>10^4$ cm^{-1}) [5]. To date, record efficiencies of 16.6%[6] on the rigid soda-lime glass (SLG) and 12.84% [7] on flexible Mo foil have been reached via a molecular ink-based absorber synthesis approach. Among kesterites, the selenium-rich $Cu_2ZnSn(S,Se)_4$ (CZTSSe) with an E_g of 1.1 eV is an ideal bottom cell candidate in flexible tandem devices incorporating perovskite top cells, thereby maximising the solar spectrum harvesting, improving the efficiency (η), and enhancing suitability for commercialisation [8,9]. Thanks to their tuneable wide bandgap, high absorption coefficient, and simple solution-based processing,

perovskite top cells have already been coupled with Si devices [10–16], reaching η of over 34%[6]. Perovskite devices in tandem configuration with inorganic thin films have drawn attention due to their potential for flexible applications, which are not feasible with Si-based tandems. Among them, perovskite/Cu(In,Ga)Se_2 (CIGS) tandem devices reported η up to 24.6%[6] on rigid substrates and over 22% on flexible ones [17], but expensive and rare constituents like In and Ga will hinder their sustainable development and consequently their successful large industrial-scale implementation. Therefore, CZTSSe is a better candidate, and its cost-effectiveness is further enhanced by synthesising it through solution-based methods [18–20]. However, the kesterite performance deficit, mainly caused by its complex defect chemistry [21–23], has limited the advancement in CZTSSe/perovskites tandem solar cells, with little research on this topic (see Figure 1). In 2014, Todorov et al. [24] for the first time demonstrated the compatibility of these two emerging PV materials, producing a proof of concept for the monolithic (2-Terminal, 2T) architecture and achieving an η of 4.6%. Notably, they attained a high open-circuit voltage (V_{OC}) of 1350 mV, close to the sum of the V_{OC} values of the single-absorber reference cells. In 2017, Li et al. [25] combined two solution-processed kesterite- and perovskite-based devices in a reflective tandem configuration, with a total η of 16.1%, higher than each of the sub-cells. In 2022, Wang et al. [26] reached an η of 22.27% in a 4-terminal (4T) tandem device configuration through an effective interfacial engineering of the wide-bandgap perovskite. This result was achieved by adopting a two-dimensional octyl-diammonium lead iodide interlayer onto the hole-transporting layer in the perovskite-based subcell. This strategy optimised the perovskite crystal growth, improved the hole extraction, and reduced the charge trap density in the top cell. In 2024, advancements in doping and alloying strategies to enhance CZTSSe device performance renewed interest in kesterite-based tandem devices, making the exploration of this topic timely and necessary. For instance, Rehan et al. [27] demonstrated a 4T architecture using CZTSe fabricated via a co-evaporation process at low temperature (480 °C) with in-situ alkali doping, achieving an η of 20.0%. Hwang et al.[28] obtained a 4T tandem efficiency of 23.01%, using a co-electrodeposited kesterite bottom cell. This result was achieved through an effective CsF treatment that improved kesterite grain growth while suppressing deep-level defects and secondary phases. Meanwhile, the same research group[29] reached a record 2T tandem efficiency of 17.5% by significantly reducing the surface roughness of the electrochemically synthesised CZTSSe. The highest reported 4T tandem efficiency of 23.96% was achieved in 2025 by Patil et al. [30], using diphenylammonium chloride as an additive

to enhance the quality of the perovskite film, improve charge carrier dynamics, and reduce non-radiative losses. However, all these studies focused on devices fabricated on rigid SLG substrates. Recently, Rehan et al. [8] produced the first 2T device on flexible polyimide (PI), reaching 11.35% efficiency. However, to avoid PI degradation, a lower-temperature process is required, which reduces kesterite grain growth and quality, consequently leading to lower PV performance[31]. Indeed, the current kesterite deposition techniques producing high-quality CZTSSe absorbers involve a high-temperature annealing step, critical for sufficient chalcogenization and crystallisation [1]. To date, the best flexible substrate choice is the high-purity and high-temperature-resistant Mo foil [32], on which CZTSSe exhibits enhanced crystallinity [33–35]. Despite these advantages, high-efficiency tandems based on the molecular-ink CZTSSe platform on flexible Mo foil substrates have remained largely unexplored. In this work, we address this gap by demonstrating molecular-ink-derived CZTSSe/perovskite 4T tandems on both rigid and flexible substrates. To further improve the quality of the absorber layer grown on flexible Mo foil substrate and consequently enhance the PV performance, artificial doping with alkaline metals (e.g. Na, Li, and K) is an effective strategy, as reported in the literature [1]. A lot of studies proved that Na, naturally present in SLG while absent in Mo foil, plays a multifunctional role in CZTSSe synthesis [1,36,37]. It promotes kesterite crystallisation and grain uniformity by acting as a fluxing agent. Additionally, Na effectively passivates grain boundaries and deep-level defects, thereby facilitating the separation of the carriers and improving the overall optoelectronic properties of the absorber. Due to the low formation energy of Na_{Cu} antisite defects, Na dopants can easily occupy Cu vacancies, which in turn inhibits the formation of detrimental Zn_{Cu}, $Cu_{Zn,}$ and related cluster defects [5,38], reducing the concentration of shallow donors in the kesterite, and finally increasing the p-type conductivity of the material [39]. Therefore, the Na incorporation is a crucial step in the CZTSSe synthesis on flexible substrates. Na can be introduced directly into the kesterite precursor ink [40,41], if the absorber is synthesised from a solution process, while it can also be deposited via sputtering or evaporation [36,38,42], if the kesterite layer is obtained via vacuum-based technologies. Other methods explored in the years involve the alkali introduction through a post-treatment strategy [7] or the design of a Na-doped Mo back contact [43]. In parallel, the isovalent cationic substitution of Cu^+ with the larger Ag^+ ion is highly effective in mitigating Cu/Zn disorder. Due to its significantly larger ionic radius, Ag increases the formation energies of antisite defects, thereby suppressing band tailing, reducing deep-level recombination centres, and promoting the formation

of more ordered kesterite domains while also facilitating grain coarsening [44–47]. In this work, Na-doping and Ag-alloying (Na-ACZTSSe) were performed to improve the kesterite morphology and grain size, yielding high-quality thin films grown on both Mo/SLG and Mo foil. When introduced together, Na and Ag act synergistically to yield high-quality thin films. While Na accelerates grain growth and passivates grain boundary defects, Ag suppresses intrinsic cation disorder and deep traps. Their combined effect leads to larger grains, reduced band tailing, and improved electronic quality of the absorber. The so-obtained high-performing kesterite bottom cells were then integrated with semi-transparent perovskite top cells into a 4T tandem architecture. The 4T tandem configuration, in which the subcells are mechanically stacked, thereby ensuring optical coupling, while remaining electrically independent, offers greater design flexibility in material selection and fabrication processes, prevents interaction between the perovskite and the bottom cell layers, eliminates the need for recombination junction and current matching, and leads to higher efficiencies compared to the 2T device. Moreover, 4T solar cells offer significant advantages for future industrial applications: since the architecture allows for independent operation of the bottom and top cells, a potentially damaged subcell can be replaced without affecting the other, thereby reducing maintenance costs. Perovskites with different E_g values and compositions were tested to ensure optimal bandgap matching between the two subcells and maximise the absorption across the electromagnetic spectrum. We have successfully demonstrated an all-solution-processed, low-cost, and efficient 4T kesterite/perovskite tandem solar cell, using a Na-ACZTSSe bottom cell grown both on Mo/SLG and Mo foil. Therefore, η exceeding 22% and 20% was reached for rigid and flexible substrates, respectively, highlighting the compatibility of these two emerging PV thin films. This solution-processed tandem approach represents a promising step toward developing cost-effective and sustainable photovoltaic technologies, with potential relevance for next-generation solar energy applications. More broadly, this work provides a proof-of-concept framework and suggests the possible feasibility of integrating solution-processed kesterite absorbers with perovskite top cells on flexible substrates, thereby opening new opportunities for lightweight and mechanically stacked tandem photovoltaics.

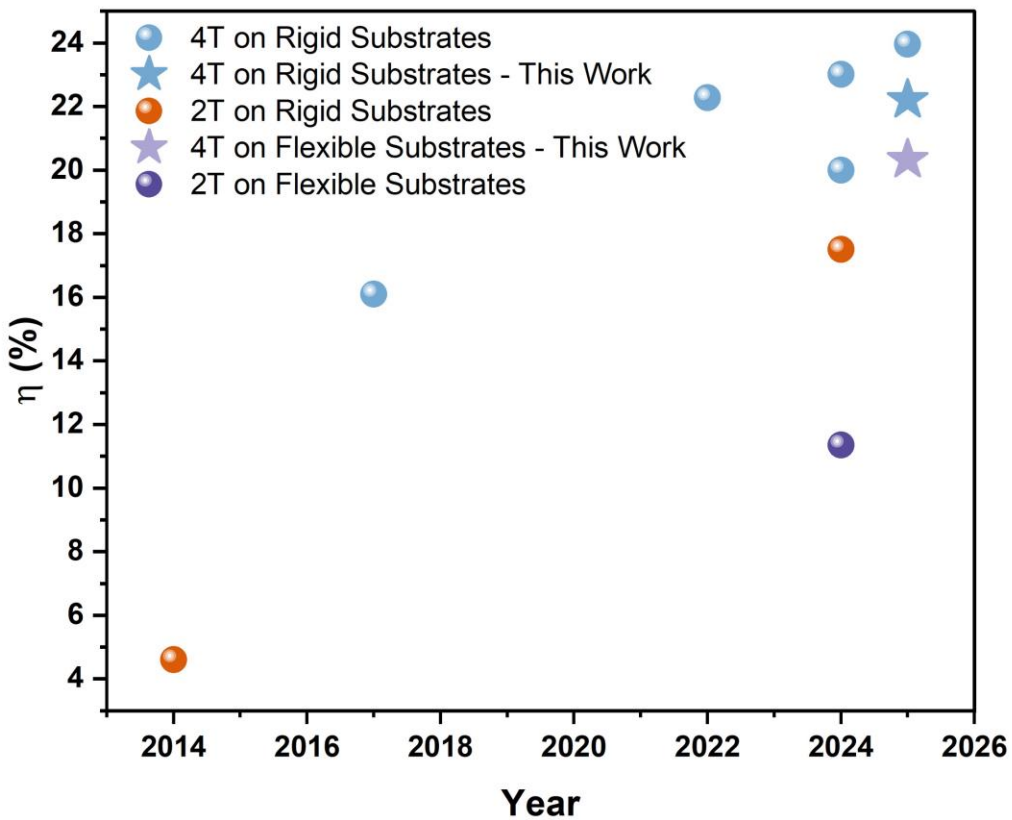

Figure 1. Efficiency evolution of tandem solar cells involving kesterite bottom cells and perovskite top cells: CZTSSe/perovskite 4T tandems on rigid substrates [25–28,30], CZTSSe/perovskite 2T tandems on rigid substrates [24,29], CZTSSe/perovskite 4T tandems on flexible substrates (this work), and CZTSSe/perovskite 2T tandems on flexible substrates [8].

Results and Discussion

Kesterite Bottom Cells Optimisation

Extensive characterisation, including SEM, X-ray diffraction (XRD), Raman spectroscopy, J-V measurements, and optical transmission/reflection analyses, was carried out to investigate the effect of Na introduction into the kesterite absorber via Na-based precursor solution, and to correlate film quality with the final device performance. In all cases (with and without Na-doping; on rigid Mo/SLG or on flexible Mo foil), the Raman spectra (Figure 2a) exhibit sharp and well-resolved peaks characteristic of the kesterite ACZTSSe phase [48,49], with no evidence of secondary phases. These results are corroborated by XRD measurements (Figure 2b), which confirm the

formation of phase-pure ACZTSSe (DB card number 00-052-0868) with high crystalline quality and no detectable secondary phases. Diffraction peaks at $2\theta = 40.8°$, 58.9°, and 73.9° are attributed to the Mo sputtered on SLG and to the Mo foil used as both substrate and back contact, respectively. Additional peaks, more intense in the flexible devices, at $2\theta = 14.0°$, 32.0°, 56.2°, and 65.8° are related to the formation of a $MoSe_2$ interlayer between the absorber and the substrate during the high-temperature annealing in a chalcogen-rich atmosphere, required for kesterite crystallisation. The XRD pattern of the Na-doped absorber layer on Mo foil exhibits a sharper and more intense 112 kesterite peak (Figure 2c), with a narrower full width at half maximum (FWHM= 0.134) compared to its undoped reference counterpart (FWHM= 0.158), indicating enhanced crystallinity and larger grain size, while for absorbers grown on Mo/SLG this effect is less evident (Figure 2d). The non-detection of secondary phases in both Raman and XRD analysis confirms the effectiveness of Na doping in improving crystallinity without modifying the precursor solution chemistry or forming detrimental by-product impurities. To assess optical properties, both Na-doped and reference absorbers were grown directly on bare SLG substrates and analysed via UV-Vis spectroscopy. As shown in Figure 2e, Tauc's plots of both films confirm the expected bandgap of approximately 1.05 eV. Top-view SEM images (Figure 3a-b) further illustrate the impact of Na introduction on the ACZTSSe morphology and grain growth on the flexible Mo foil. The undoped reference absorber film grown on Mo foil (Figure 3a) displays irregular grains (typically exceeding 1-2 μm in size), along with small voids/cavities and several grain boundaries, which likely promote carrier recombination and limit PV performance. In contrast, Na doping favoured grain coarsening, yielding larger grains (over 2-3 μm in lateral extension), densely packed morphology, and reduced grain boundary density, as shown in Figure 3b. The better kesterite morphology, characterised by improved crystallinity and enlarged grain sizes, aligns with the XRD results. These findings highlight the key role of alkali doping in promoting crystallisation during film growth on flexible substrates. This is consistent with previous studies [50–53] showing that Na dopant promotes the formation of sodium-polyselenides (Na_2Se_x) liquid phases at the grain boundaries during selenization, which drives grain growth and enhances the crystallinity of ACZTSSe films (Figure 3c-d). Cross-section SEM images (Figure 3e-f) of the samples deposited on rigid SLG show that the morphology of the Na-doped absorbers is similar to that of the undoped reference sample. This indicates that, in this case, Na introduced directly into the solution does not significantly improve the crystallinity. This result suggests that, despite the presence of the SiO_x barrier, lateral diffusion

of Na from the substrate into the CZTSSe film likely occurs during the high-temperature annealing, thereby limiting the effect of the Na dopant introduced directly in solution. The beneficial effect of Na-doping mainly originates from improved crystallisation and grain coarsening of the CZTSSe absorber, especially on flexible Mo foil, where no Na is supplied by the substrate. The enlarged grains and reduced grain-boundary density are expected to suppress recombination losses and improve carrier transport, which is consistent with the observed enhancement in V_{OC}, fill factor (FF), and overall device efficiency, as discussed in the following paragraph.

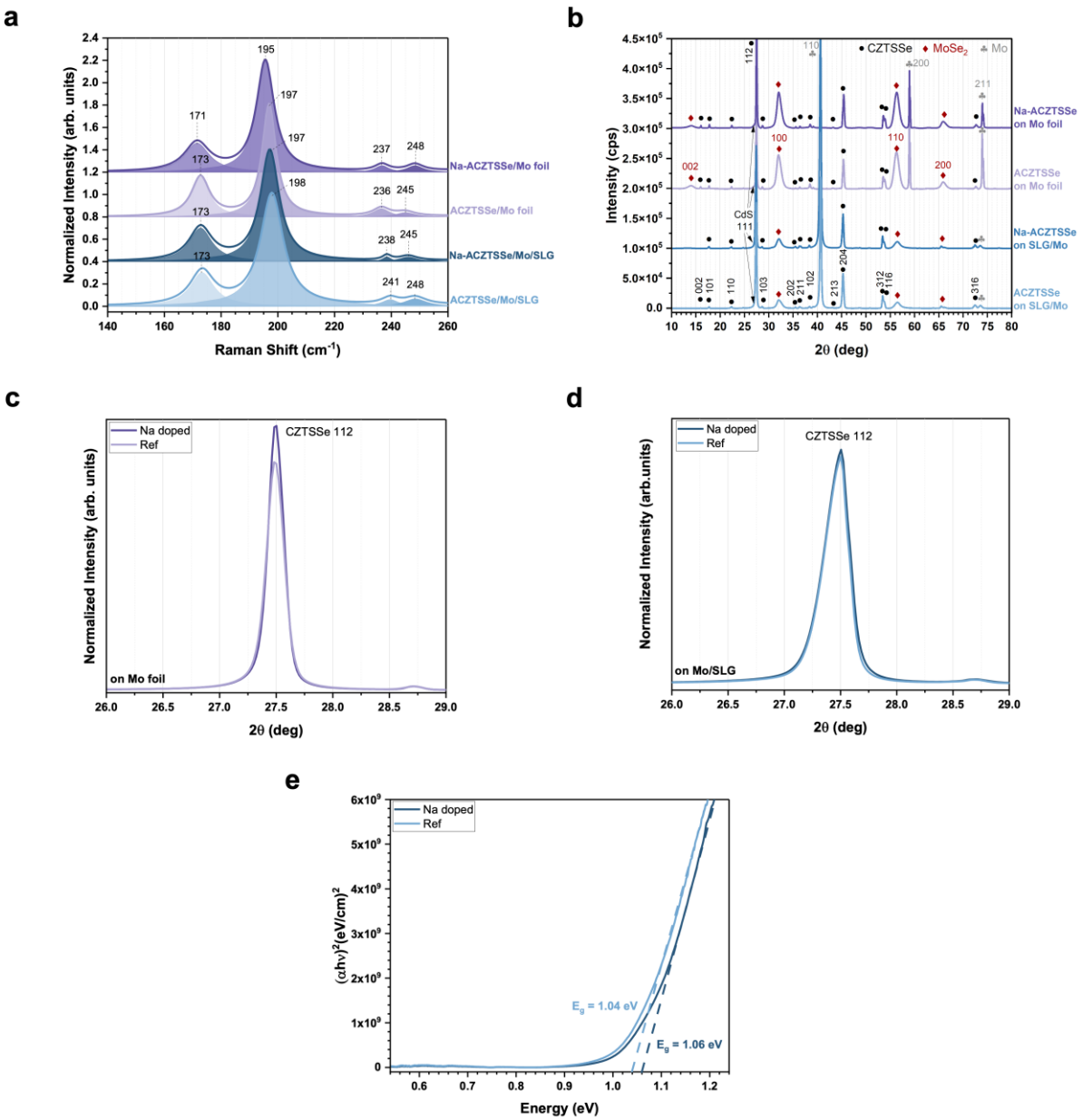

Figure 2. (a) Raman spectra, (b) X-Ray diffraction patterns, zoomed 112 kesterite XRD peaks from panel (b) illustrating variations in peak intensity and FWHM on (c) flexible Mo foil and (d) on Mo/SLG, and (d) Tauc's plot of reference ACZTSSe (in light blue) and Na-ACZTSSe (in dark blue) samples.

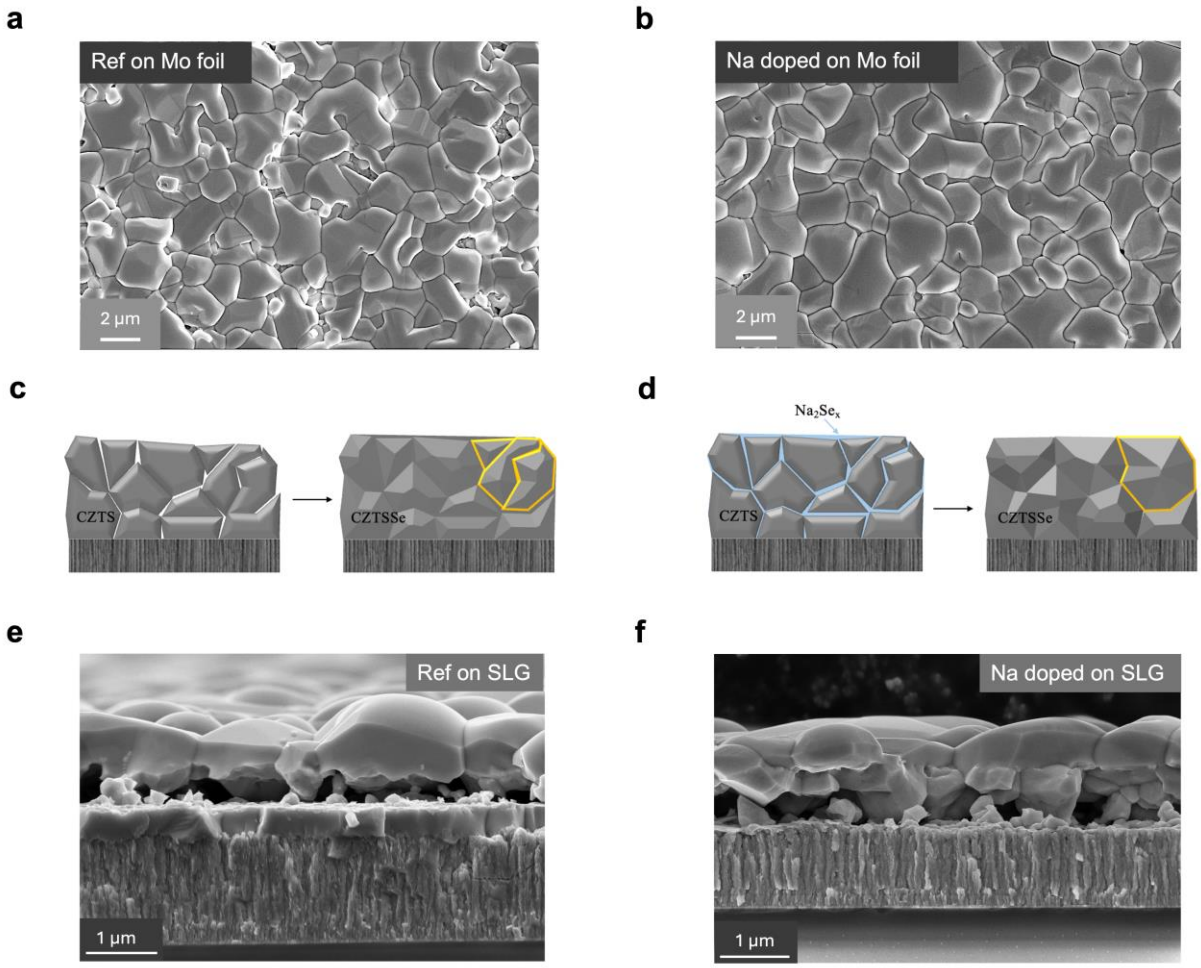

Figure 3. Top-view SEM images of (a) the reference absorber and (b) the Na-doped one grown on Mo foil. Schematic illustration of the kesterite grain growth during the high-temperature annealing (c) without and (d) with Na as a dopant. Cross-section SEM images of (e) the undoped absorber and (f) the Na-doped one deposited on Mo-coated SLG.

Statistical box plots of short-circuit current density (J_{SC}), V_{OC}, FF, and η (Figure 4a-d) demonstrate the significant impact of alkali doping on device performance. Na-ACZTSSe-based samples exhibited improved PV parameters, most notably FF and η. In agreement with the SEM images, this phenomenon is more evident for devices on flexible Mo foil. These enhancements suggest that the Na doping improves charge carrier transport, mitigates carrier recombination, and reduces device resistance, thanks to larger grain size and lower grain boundary density in the absorber layer. The Na-doping yielded the highest values for V_{OC} (532 mV), J_{SC} (34.19 mA/cm^2), FF

(59.26%), and η (10.79%) on rigid Mo/SLG, and V_{OC} (499 mV), J_{SC} (36.36 mA/cm^2), FF (54.2%), and η (9.84%) on flexible Mo foil. The observed efficiency gap between rigid and flexible substrates can be attributed to the intrinsic properties of the back contacts. As also reported in our previous paper [54], compared with sputtered Mo on SLG, flexible Mo foil is rougher, more chemically reactive, and more prone to stress during high-temperature selenization, which promotes excessive $MoSe_2$ formation, local strain accumulation, cation interdiffusion, and less controlled grain growth, thereby increasing interfacial and grain-boundary recombination. In addition, although the same $NaClO_4$ content was introduced into both precursor solutions and a SiO_X barrier was used on SLG, the rigid substrate may still receive additional Na from lateral diffusion at the glass edges, contributing to superior grain coarsening and lower recombination than on Mo foil. Future improvements may therefore rely on interfacial engineering to regulate $MoSe_2$ growth and mechanical stress, together with further alkali co-doping optimisation.

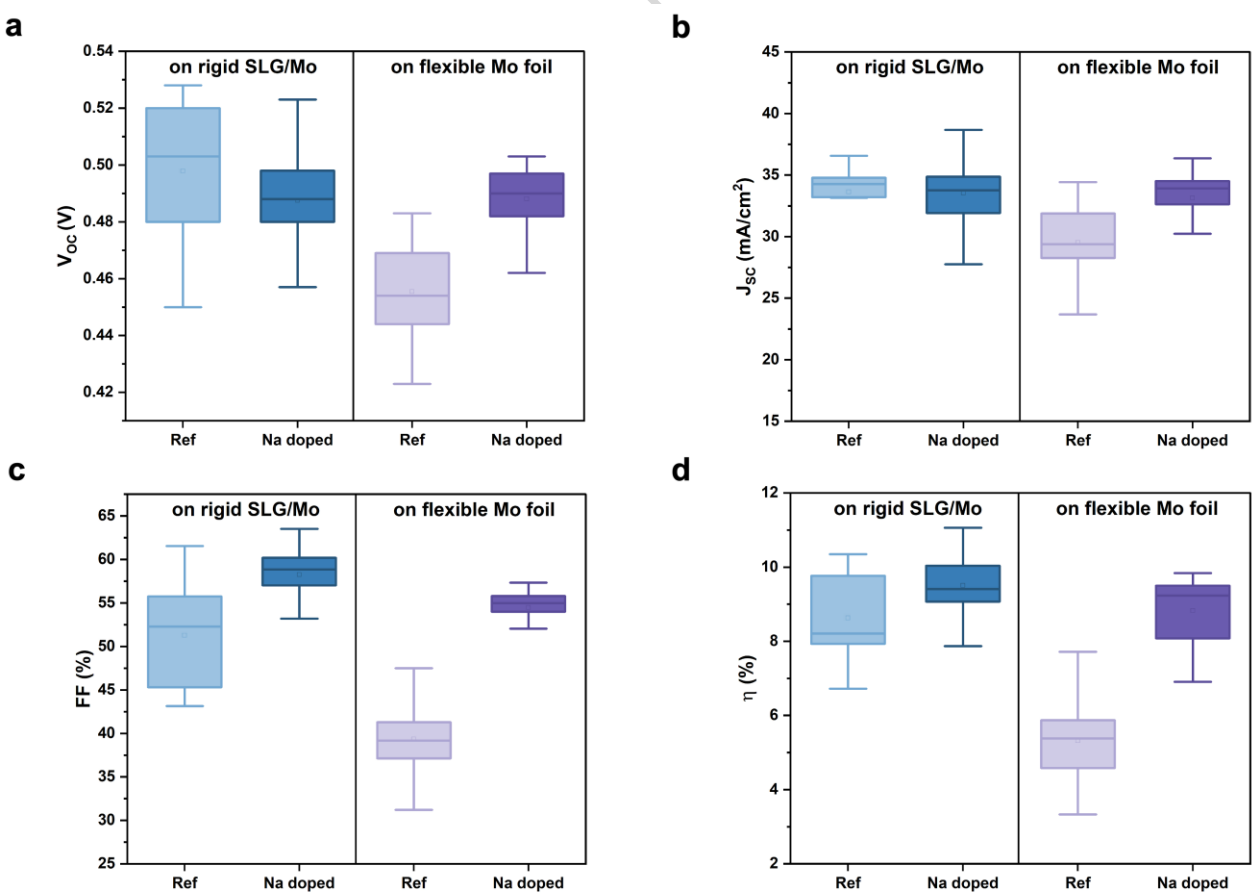

Figure 4. Box plots highlighting the statistical distributions of (a) V_{OC}, (b) J_{SC}, (c) FF, and (d) η for the samples grown on SLG/Mo and Mo foil, with and without Na-doping of ACZTSSe. Each condition includes 20 solar cells.

Rigid Kesterite/Perovskite 4-Terminal Tandem Devices

The so-obtained rigid devices were then integrated as bottom cells into a 4T tandem configuration with perovskite-based top cells. To ensure optimal bandgap matching between bottom and top cells and maximise the harvest across the AM1.5G spectrum, perovskites with different compositions and device architecture were tested (Figure 5a-c). $FAPbBr_3$ with a 2.3 eV bandgap, $Cs_{0.17}FA_{0.83}Pb(I_{0.75}Br_{0.25})_3$ with a 1.68 eV bandgap, and $Cs_{0.17}FA_{0.83}Pb(I_{0.90}Br_{0.10})_3$ with a 1.63 eV bandgap, all in the optimal range for 4T with Na-ACZTSSe with E_g= 1.05 eV, were selected for this purpose. Rather than a narrow compositional tuning around a specific bandgap, these representative semitransparent perovskites were chosen to quantify the fundamental trade-off between top-cell performance and optical filtering losses affecting the kesterite bottom cell. The perovskite cells were measured in both forward (FW) and reverse (RV) scan modes. The detailed PV parameters of the perovskite cells are reported in Table 1 and in Figure S1. For each type, the best-performing perovskite cell was used as a filter on top of the champion kesterite bottom cell. A schematic representation of the 4T device architecture used, in which the two subcells are individually fabricated and then mechanically stacked on top of each other, is depicted in Figure 6a. This 4T configuration allows the subcells to remain electrically independent and physically separated, effectively avoiding tandem-specific degradation pathways that typically arise in monolithic architectures from direct interconnection or interlayer chemical interactions. Therefore, the tandem stability is primarily governed by the intrinsic durability of the individual devices. As the wide-bandgap perovskite top cell is typically considered the bottleneck for tandem operational life, it is important to highlight that the compositions selected for this study have previously demonstrated over 1000 h of stability under continuous light soaking, suggesting their potential for long-term tandem applications[55,56]. Furthermore, the kesterite bottom cell is based on an inherently robust inorganic semiconductor with well-documented long-term stability [54,57].

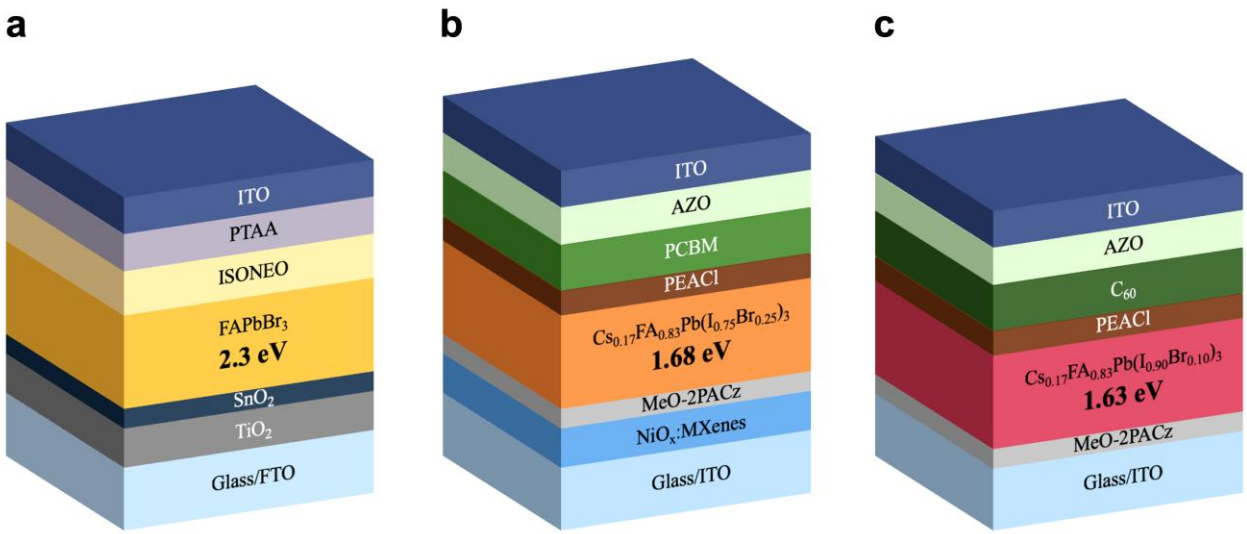

Figure 5. Schematic architecture of the perovskite top cells based on (a) $FAPbBr_3$, (b) $Cs_{0.17}FA_{0.83}Pb(I_{0.75}Br_{0.25})_3$, (c) $Cs_{0.17}FA_{0.83}Pb(I_{0.90}Br_{0.10})_3$.

Table 1. PV performance of the rigid perovskite cells. Reported values include the average, standard deviation, and best-performing cell, both in forward (FW) and reverse (RV) scan modes.

Top cell	E_g (eV)	Scan mode	V_{OC} (V)	J_{SC} (mA/cm^2)	FF (%)	η (%)
$FAPbBr_3$ (Rigid)	2.3	FW	1.55 ± 0.03 (1.49)	6.08 ± 0.54 (6.68)	63.2 ± 3.7 (63.1)	5.97 ± 0.77 (6.32)
		RV	1.55 ± 0.02 (1.50)	6.08 ± 0.53 (6.66)	66.6 ± 2.3 (68.9)	6.28 ± 0.47 (6.89)
$Cs_{0.17}FA_{0.83}Pb(I_{0.75}Br_{0.25})_3$ (Rigid)	1.68	FW	1.110 ± 0.005 (1.110)	18.16 ± 0.38 (18.42)	74.95 ± 1.3 (79.7)	15.20 ± 0.40 (16.40)
		RV	1.110 ± 0.004 (1.110)	18.20 ± 0.38 (18.47)	75.3 ± 1.1 (79.5)	15.31 ± 0.35 (16.42)
$Cs_{0.17}FA_{0.83}Pb(I_{0.90}Br_{0.10})_3$ (Rigid)	1.63	FW	1.062 ± 0.001 (1.061)	22.41 ± 0.05 (22.35)	79.9 ± 1.4 (81.0)	18.99 ± 0.33 (19.30)
		RV	1.064 ± 0.002 (1.060)	22.42 ± 0.05 (22.42)	80.0 ± 1.5 (82.0)	19.06 ± 0.33 (19.44)

As shown in Figure 6b-e, the top cells absorb and convert short-wavelength light into electricity, depending on the perovskite E_g, while lower-energy photons are transmitted and absorbed by the kesterite bottom cells. This strategy enables broader harvesting of the solar spectrum. The EQE spectra of the kesterite bottom cell under the perovskite filters confirm no spectral response in the region between 300 nm and 600-800 nm, consistent with photon absorption and conversion occurring in the top cell. Due to this filtering effect, the integrated J_{SC} of the kesterite bottom cell decreases from its standalone value of 33.40 mA/cm^2 to 21.96 mA/cm^2, 15.68 mA/cm^2, and 10.35 mA/cm^2 when filtered by $FAPbBr_3$, $Cs_{0.17}FA_{0.83}Pb(I_{0.75}Br_{0.25})_3$, and $Cs_{0.17}FA_{0.83}Pb(I_{0.90}Br_{0.10})_3$, respectively. As the perovskite bandgap narrows, its spectral overlap with the kesterite bottom cell increases, intensifying the filtering effect. Moreover, the filtered bottom cell shows a reduced photoresponse in the near-infrared (NIR, over 800 nm) region compared to the single junction Na-

ACZTSSe device. As shown by the transmittance spectra in Figure 6f, this attenuation is directly linked to the optical transparency of the complete top cell stack, including all functional layers and transparent electrodes, which determines the photon flux reaching the bottom kesterite device. In particular, for the $Cs_{0.17}FA_{0.83}Pb(I_{0.90}Br_{0.10})_3$-based top cell, which exhibits the most pronounced filtering effect, the average transmittance in the NIR region (800–1200 nm) is approximately 59%, corresponding to parasitic optical losses of about 41%. These losses originate mainly from absorption and reflection within the transparent electrodes and charge-transport layers, such as ITO and fullerene-based interfaces, rather than the perovskite itself, whose absorption edge lies below the NIR region [28,29]. These losses could be mitigated by adopting a 2T tandem architecture, eliminating the need for an ITO/glass substrate in the perovskite top cell. While these modifications alleviate some of the concerns with mechanical integrity, other limitations of fullerenes remain, including poor band alignment with wide gap perovskites, parasitic absorption in tandems, permeability, and cost[58]. Figure 6g illustrates the J-V characteristics of the bottom cell under different filtering conditions, while Table 2 summarises the corresponding PV parameters. When coupled with the perovskite top cells, the Na-ACZTSSe-based devices achieved η of 7.02%, 4.39% and 2.91% using $FAPbBr_3$, $Cs_{0.17}FA_{0.83}Pb(I_{0.75}Br_{0.25})_3$, and $Cs_{0.17}FA_{0.83}Pb(I_{0.90}Br_{0.10})_3$ as filters, respectively. The efficiency reduction is primarily due to a decrease in J_{SC} caused by the filtering effect, which is in agreement with the EQE data. A slight drop in V_{OC} (~ 40 mV) and FF (~ 3%) is also observed, likely due to the lower light intensity reaching the bottom cell compared to the standalone Na-ACZTSSe device, which reduces the photo-induced charge carrier concentration[26]. The combined $FAPbBr_3$, $Cs_{0.17}FA_{0.83}Pb(I_{0.75}Br_{0.25})_3$ and $Cs_{0.17}FA_{0.83}Pb(I_{0.90}Br_{0.10})_3$ based top cells and the filtered kesterite bottom cells yielded a final 4T η, calculated as the sum of the efficiencies of the individual subcells, of 13.34%, 20.79%, 22.21%, respectively. In all cases, the overall 4T efficiency surpassed that of both standalone subcells. Notably, when using $Cs_{0.17}FA_{0.83}Pb(I_{0.90}Br_{0.10})_3$ (1.63 eV) as a filter, the high efficiency of the perovskite top cell dominates the overall performance and compensates for the stronger filtering effect on the bottom cell, resulting in the highest 4T efficiency observed in this study (Figure 6h). Moreover, this result ranks among the highest reported in the literature for devices fabricated on rigid substrates (Figure 1).

Flexible Kesterite/Perovskite 4-Terminal Tandem Devices

The optimised 4T tandem architecture was then transferred to flexible substrates, as illustrated in Figure 7a. In this configuration, the $Cs_{0.17}FA_{0.83}Pb(I_{0.90}Br_{0.10})_3$-based solar cell was fabricated on flexible PET/ITO, while the kesterite bottom cell was grown on Mo foil, as discussed above. The selection of these substrates is supported by their established mechanical robustness under repeated bending cycles, maintaining high performance retention even at reduced bending radii [54,59–61]. Specifically, the mechanical integrity of the kesterite-based bottom cells was investigated in our previous study [54], demonstrating an efficiency retention exceeding 90% after 500 cycles at a 1.0 cm radius. The observed high stability of both V_{OC} and FF highlights the resilience of the kesterite/substrate interface against mechanical strain-induced delamination or cracking, attributed to the incorporation of the engineered MoO_3 back interface, thereby suggesting the feasibility of flexible tandem operation. The PV parameters of the flexible perovskite cells, including average values, standard deviations, and the best-performing cell used in the 4T configuration, are reported in Table 3 and in Figure S1. The EQE spectra and the J-V curves of the stand-alone and filtered bottom and top cells are presented in Figure 7b-c. When inserted in the 4T tandem configuration with the best-performing flexible perovskite top cell (η= 18.07%), the champion kesterite-based bottom cell (η= 9.84%) achieved an η of 2.26%. All PV parameters of the Na-ACZTSSe single-junction device showed a slight reduction upon insertion into the tandem architecture, as reported in detail in Table 4. This efficiency drop is consistent with the EQE data: the filtered kesterite bottom cell exhibits no spectral response in the region of 300-800 nm and shows additional parasitic absorption losses in the NIR region (Figure 7d). For the flexible $Cs_{0.17}FA_{0.83}Pb(I_{0.90}Br_{0.10})_3$-based top cell on PET/ITO, the average NIR transmittance is 54%, resulting in parasitic optical losses of 46%, in agreement with the results observed for devices on rigid substrates. Despite these losses, the flexible 4T Na-ACZTSSe/ $Cs_{0.17}FA_{0.83}Pb(I_{0.90}Br_{0.10})_3$ tandem device achieved an overall η of 20.33%, which is calculated as the sum of the efficiencies of the two subcells. To the best of our knowledge, this represents the highest efficiency reported for 4T kesterite/perovskite tandem solar cells on flexible substrates, highlighting the potential of this approach in a proof-of-concept demonstration.

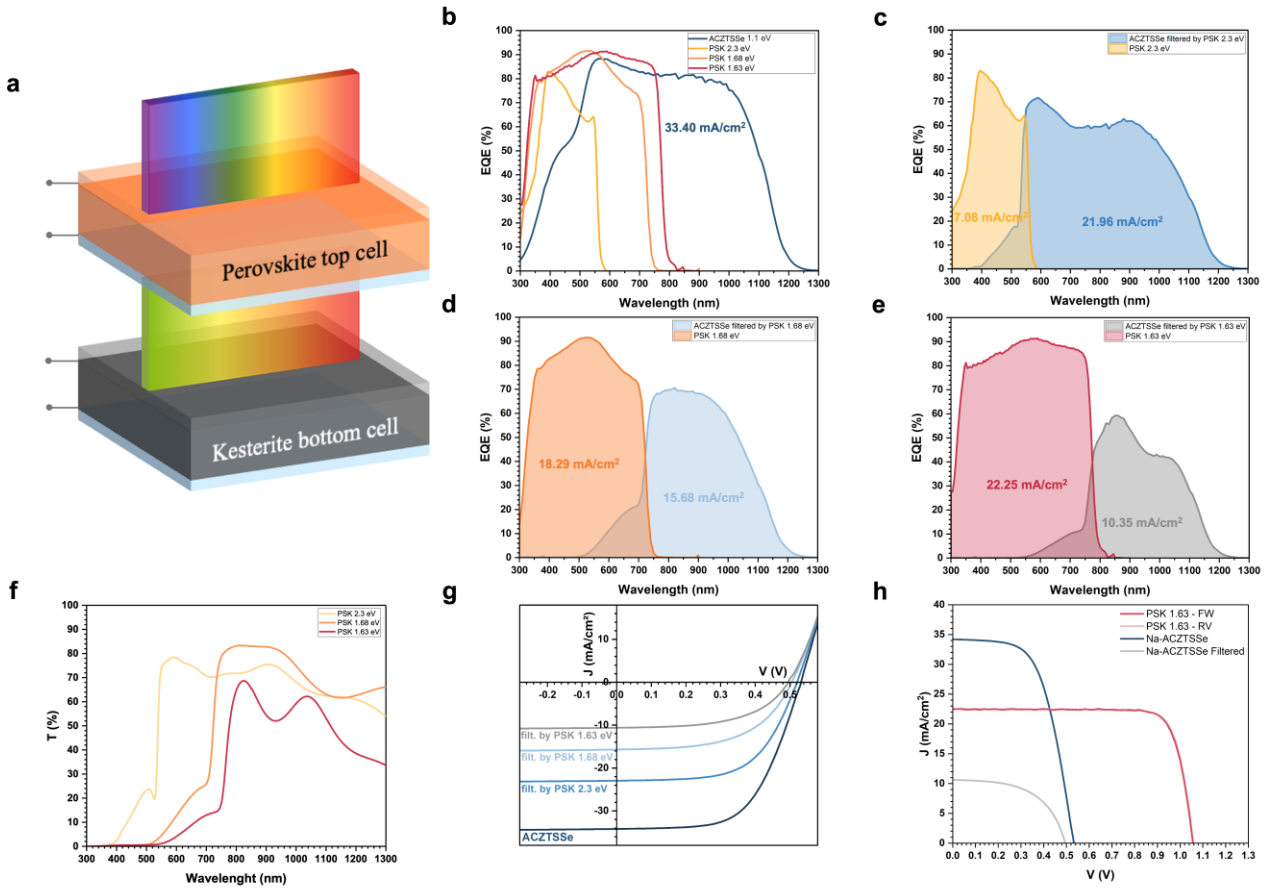

Figure 6. (a) Device architecture of rigid perovskite/kesterite 4T tandem solar cells. (b) EQE spectra of the different perovskite-based top cells and the kesterite-based bottom cell. Comparison between (c) $FAPbBr_3$, (d) $Cs_{0.17}FA_{0.83}Pb(I_{0.75}Br_{0.25})_3$ and (e) $Cs_{0.17}FA_{0.83}Pb(I_{0.90}Br_{0.10})_3$ EQE spectra and the corresponding filtered Na-ACZTSSe bottom cell. (f) Transmittance of the perovskite filters. (g) J-V characteristic of the kesterite bottom cell under different filtering conditions and (h) of the $Cs_{0.17}FA_{0.83}Pb(I_{0.90}Br_{0.10})_3$ cell.

Table 2. Photovoltaic parameters of the best-performing kesterite bottom cell (stand-alone and filtered by different perovskite (PSK) top cells) and 4T tandem solar cells on rigid substrates, measured in forward scan mode.

Rigid devices	V_{OC} (mV)	J_{SC} (mA/cm^2)	FF (%)	η (%)	E_g (eV) PSK	η (%) PSK filter	η (%) tandem 4T

Na-ACZTSSe	532	34.19	59.26	10.79	-	-	-
Na-ACZTSSe filtr. by $FAPbBr_3$	520	22.59	59.81	7.02	2.3	6.32	13.34
Na-ACZTSSe filtr. by $Cs_{0.17}FA_{0.83}Pb(I_{0.75}Br_{0.25})_3$	505	15.68	55.44	4.39	1.68	16.40	20.79
Na-ACZTSSe filtr. by $Cs_{0.17}FA_{0.83}Pb(I_{0.90}Br_{0.10})_3$	494	10.46	56.25	2.91	1.63	19.30	22.21

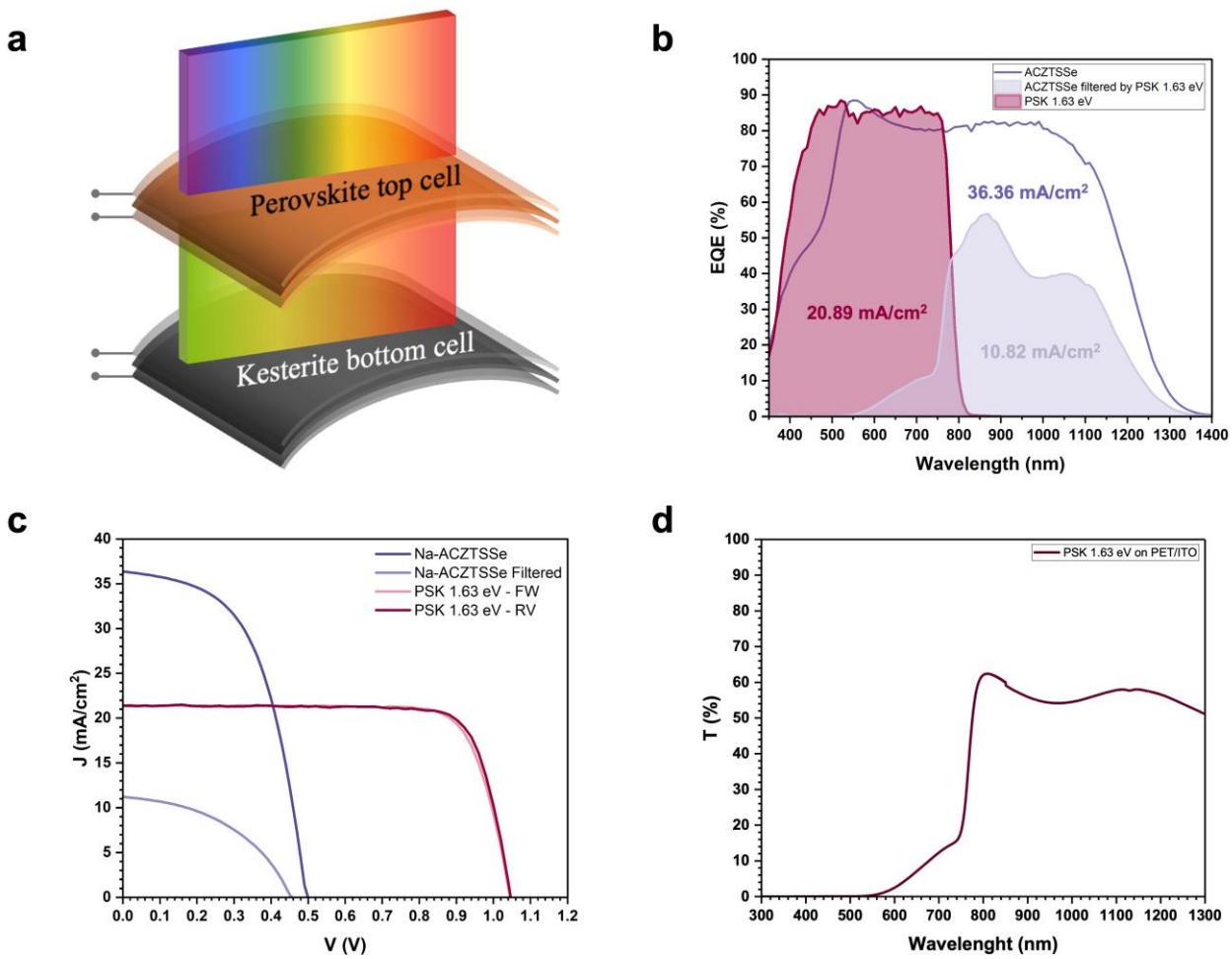

Figure 7. (a) Device architecture of flexible perovskite/kesterite 4T tandem solar cells. (b) EQE spectra and (c) J-V characteristic of the flexible $Cs_{0.17}FA_{0.83}Pb(I_{0.90}Br_{0.10})_3$-based top cell and of the stand-alone and filtered flexible kesterite-based bottom cell. (d) Transmittance of the flexible perovskite top cell.

Table 3. PV performance of the flexible perovskite-based cells. Reported values include the average, standard deviation, and best-performing cell, both in forward (FW) and reverse (RV) scan modes.

Top cell	E_g (eV)	Scan mode	V_{OC} (V)	J_{SC} (mA/cm^2)	FF (%)	η (%)
$Cs_{0.17}FA_{0.83}Pb(I_{0.90}Br_{0.10})_3$ (Flexible)	1.63	FW	1.042 ± 0.003 (1.044)	21.69 ± 0.10 (21.74)	78.1 ± 1.2 (79.6)	17.65 ± 0.30 (18.07)
		RV	1.045 ± 0.004 (1.050)	21.73 ± 0.10 (21.81)	78.2 ± 1.2 (79.7)	17.83 ± 0.32 (18.25)

Table 4. Photovoltaic performance of the best-performing kesterite bottom cell (stand-alone and filtered by $Cs_{0.17}FA_{0.83}Pb(I_{0.90}Br_{0.10})_3$) and 4T tandem solar cell on flexible substrates, measured in forward scan mode.

Flexible devices	V_{OC} (mV)	J_{SC} (mA/cm^2)	FF (%)	η (%)	E_g (eV)
Na-ACZTSSe	499	36.36	54.20	9.84	1.05
Na-ACZTSSe filtr. by PSK	456	11.21	44.25	2.26	-
4T tandem device	-	-	-	20.33	-

Conclusion

In summary, this work presents a promising solution-based strategy to produce both rigid and flexible high-efficiency kesterite solar cells. Na-doping was found to be an effective method for enhancing the crystallinity, morphology, and overall PV performance of the kesterite-based devices. An all-solution-processed, low-cost, and efficient 4T tandem device configuration, combining a narrow-bandgap kesterite (Na-ACZTSSe) bottom cell and a wide-bandgap perovskite top cell, has been successfully developed. This tandem architecture achieved an overall η exceeding 22% on rigid substrates and over 20% on flexible ones, which, to the best of our knowledge, is the highest reported in the literature for such devices. This work provides a proof-

of-concept efficiency demonstration of a 4T kesterite/perovskite tandem solar cell on flexible substrates, highlighting the potential of this approach. The best-performing configuration used $Cs_{0.17}FA_{0.83}Pb(I_{0.90}Br_{0.10})_3$ as the top cell, leveraging its higher efficiency to compensate for the filtering effect on the kesterite-based bottom cell. These results support the compatibility and highlight the synergistic efficiency potential of the tandem application of kesterite and perovskite, two leading emerging thin-film PV technologies. Notably, using lightweight, bendable substrates enables new opportunities for next-generation applications, such as product- and building-integrated PV, and the tandem approach provides a strategic shortcut to commercialisation. Additionally, the solution-based approach offers a scalable and industrially appealing fabrication route, minimising reliance on vacuum-based or high-cost techniques, while maintaining high PV performance. To conclude, this work provides a relevant demonstration for advancing lightweight, bendable, and high-performance tandem solar cells, supporting their potential in PV applications where mechanical flexibility, low weight, and high efficiency are essential. While more challenging due to current matching requirements and the need to design an efficient recombination junction, this study, by leveraging the demonstrated materials compatibility and processing insights, paves the way for future development of flexible monolithic 2T kesterite/perovskite tandem solar cells.

Methods

Kesterite substrate preparation

Commercially available Mo foils were used as flexible substrates. The foils were first cut into 2.5 cm × 2.5 cm × 0.1 mm samples and mechanically flattened using a cold press (10 tons, 1 min) to achieve a uniform surface, minimise macro-scale irregularities, and make it suitable for solution processing. As reference substrates, 2.5 cm × 2.5 cm × 2.0 mm Mo-coated SLG were used too. To regulate Na incorporation and prevent uncontrolled alkali out-diffusion from the glass bulk, SLG substrates with a SiO_x barrier layer were used. The substrates were cleaned in an ultrasonic bath with an Alconox® detergent solution and deionised water, and finally dried under a nitrogen flow. Then, the so-cleaned flexible substrates were annealed on a hot plate (450 °C, 10 min) under ambient atmosphere to synthesise a MoO_3 interlayer. This oxide layer acts as a sacrificial and functional barrier to moderate the reaction between the Mo foil and the chalcogen atmosphere. It

also suppresses the undesired diffusion of kesterite metal cations into the Mo foil, thereby preventing the decomposition of the absorber at the back interface[54]. Furthermore, MoO_3 significantly improves the substrate wettability, leading to a more compact and uniform precursor film[54].

Na-ACZTSSe thin film preparation

The molecular ink was prepared in ambient air. First, Thiourea (TU) [2.76 M], CuCl [0.59 M], and AgCl [0.066 M] were dissolved in 2-Methoxyethanol (MOE) under stirring at 80 °C, to obtain the TU-Cu-Ag solution. Then $SnCl_4$ [0.42 M], $Zn(CH_3CO_2)_2$ [0.46 M], and $NaClO_4 \cdot H_2O$ [0.1 M] were added. After complete dissolution, the precursor solution was filtered through a 0.45 µm Nylon filter and deposited on the Mo foil substrates via spin-coating (4000 rpm for 30 s). The samples were then dried on a hot plate at 300 °C for 2 min to form a solid precursor film. This deposition-drying process was repeated 8 times to obtain the final desired thickness of 1-1.1 µm. The precursor films were then placed in a graphite box (36 cm^3) containing 480 mg of Se pellets and annealed in a tubular furnace (tube volume of 5000 cm^3) under N_2 atmosphere. The films were annealed in a chalcogenide-rich atmosphere to promote absorber crystallisation and grain growth. The final annealing temperature of 580 °C was reached in 30 minutes and kept for 20 minutes.

Na-ACZTSSe Device fabrication

The kesterite-based samples were then completed as PV devices (Figure 8a-b), depositing 50 nm of CdS via chemical bath deposition (CBD), 80 nm of i-ZnO, 150 nm of In_2O_3:SnO_2, 90:10 (ITO) through magnetron sputtering, and 500 nm of Ag electrode by thermal evaporation. Finally, to minimise reflection losses at the front surface and further increase the photocurrent and the overall performance, a 105 nm thin MgF_2 antireflective coating (ARC) was deposited by thermal evaporation.

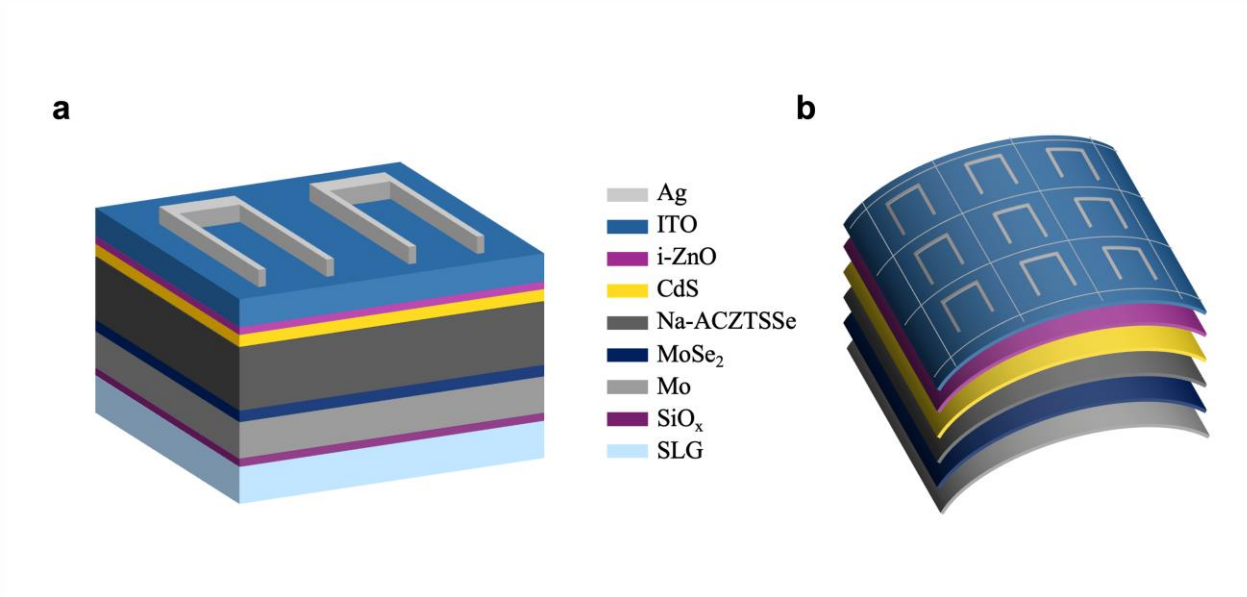

Figure 8. Schematic representation of the kesterite-based solar cells grown on (a) rigid SLG and (b) flexible Mo foil.

Perovskite-based Devices

Semi-transparent $FAPbBr_3$ solar cells were fabricated with the device architecture glass/FTO/c-TiO_2/SnO_2/$FAPbBr_3$/ISONEO/PTAA/ITO. The $Cs_{0.17}FA_{0.83}Pb(I_{0.75}Br_{0.25})_3$-based solar cells employed the structure glass/ITO/NiO_x:MXenes/MeO-2PACz/$Cs_{0.17}FA_{0.83}Pb(I_{0.75}Br_{0.25})_3$/PEACl/PCBM/AZO/ITO/$MgF_2$, while the $Cs_{0.17}FA_{0.83}Pb(I_{0.90}Br_{0.10})_3$ based devices followed the stack glass/ITO/MeO-2PACz/ $Cs_{0.17}FA_{0.83}Pb(I_{0.90}Br_{0.10})_3$/PEACl/$C_{60}$/AZO/ITO. This last architecture was then transferred onto PET/ITO flexible substrate. These device architectures slightly differ to maximise charge extraction from each perovskite composition, tailoring the layers to optimise performance for the specific halide ratio and cation mix.

$FAPbBr_3$ Device Fabrication

Glass substrates coated with fluorine-doped tin oxide (FTO) were patterned using a pulsed UV Nd:YVO_4 laser system (Luce 40, BrightSolutions), following a P1 scribing process to selectively remove the FTO layer and electrically isolate the photoelectrode from the counter electrode. The substrates were first cleaned using a diluted detergent solution (2% Hellmanex in deionized water),

followed by ultrasonic cleaning at 40 °C in ethanol and isopropanol (IPA), each for 10 minutes. Before deposition of the electron transport layer (ETL), the patterned substrates underwent UV/ozone treatment using a PSD Pro Series Digital UV Ozone System (Novascan) to eliminate organic surface residues. Compact TiO_2 (c-TiO_2) ETLs were deposited via spray pyrolysis. A precursor solution containing 0.16 M titanium diisopropoxide bis(acetylacetonate) and 0.4 M acetylacetone in ethanol was sprayed onto the preheated FTO substrates at 460 °C. The process involved 10 spray cycles, spaced 10 seconds apart, using air as the carrier gas at 1.6 bar pressure and a spray angle of approximately 45°. After deposition, the substrates were kept at 460 °C for 10 additional minutes before cooling. A dispersion of SnO_2 nanoparticles diluted 1:20 v/v in deionised water was then spin-coated onto the TiO_2 layer at 4000 rpm for 20 seconds, followed by annealing at 120 °C for 20 minutes. For the fabrication of $FAPbBr_3$-based perovskite layers, a 1 M solution of the precursor in dimethyl sulfoxide (DMSO) was prepared. In a nitrogen-filled glovebox, substrates were heated to 60 °C, and 80 µL of the solution was spin-coated at 4000 rpm for 20 seconds. At the 10-second mark, 200 µL of ethyl acetate was dropped as an antisolvent to trigger crystallisation. The resulting films were annealed at 80 °C for 10 minutes. To passivate the surface, a thin 2D layer named ISONEO was applied; this was formed by mixing two solutions—neo-pentylammonium chloride (NEO) and iso-pentylammonium chloride (ISO)—each prepared at 1 mg/mL in IPA, in a 1:1 volume ratio. The mixture was spin-coated at 4000 rpm for 20 seconds. The hole transport layer (HTL) was created by spin coating 90 µL of poly(triarylamine) (PTAA) solution (10 mg/mL), also at 4000 rpm for 20 seconds. The PTAA solution was doped with 5 µL/mL of lithium bis(trifluoromethanesulfonyl)imide (LiTFSI), from a stock solution of 170 mg/mL in acetonitrile, and 10 µL/mL of 4-tert-butylpyridine (tBP). Finally, a transparent 100 nm thick indium tin oxide (ITO) electrode was deposited via inline magnetron sputtering (KENOSISTEC S.R.L., KS 400 In-Line) at low temperature using 90 W RF power and a chamber pressure of 1.1×10^{-3} mbar. Argon gas was introduced at a 40 sccm flow rate to initiate plasma generation. The sample holder completed 200 passes beneath the sputtering target at a speed of 120 cm/min. The resulting ITO layer exhibited a sheet resistance of 30 Ω/□, measured using a four-point probe system. Further details have already been reported in a previous work [62].

$Cs_{0.17}FA_{0.83}Pb(I_{0.75}Br_{0.25})_3$ Device Fabrication

The detailed fabrication process has been previously reported [56]. A UV nanosecond laser was used to perform the P1 process on Glass/ITO (2.5 × 2.5 cm^2). Substrates were sequentially cleaned with deionised water, IPA, and ethanol (10 min for each step), followed by UV/ozone treatment for 15 minutes. Nickel oxide-nanoparticles (NiO_x-np) were dispersed in pure water (20 mg/ml). A 0.95:0.05 NiO_x:Nb-MXene dispersion was then prepared and blade-coated onto ITO. The distance between the glass/ITO and the knife of the blade was set to 200 µm, and the speed was 15 mm/s. The resulting HTL was then annealed at 150 °C for 10 minutes. After cooling, substrates were transferred into a nitrogen-filled glovebox. 150 µl of 0.5 mg/ml MeO-2PACz in ethanol was spin-coated on the NiO_x:Nb-Mxene layer at 5000 rpm for 30 seconds, followed by annealing at 100 °C for 10 minutes. The perovskite precursor solution was prepared using 1.2 M $Cs_{0.17}FA_{0.83}Pb(_{0.75}Br_{0.25})_3$ in a dimethylformamide (DMF):DMSO 4:1 solvent mixture. A 100 µl volume of this solution was spun at 4000 rpm for 35 seconds. During the last 15 s of spin coating, 150 µl of chlorobenzene (CB) was dispensed as an antisolvent. Finally, the film was annealed at 100 °C for 20 minutes. A 2 mg/ml solution of phenethylammonium chloride (PEACl) in IPA was spun on top of the perovskite layer at 6000 rpm for 25 seconds, followed by annealing at 100 °C for 5 minutes. Subsequently, 85 µl of a 27 mg/ml [6,6]-phenyl-C_{61}-butyric acid methyl ester (PCBM) solution in a 0.75:0.25 CB:dichlorobenzene (DCB) volume ratio was spin-coated dynamically at 2000 rpm for 30 seconds and then annealed at 100 °C for 5 minutes. To complete the device, Al:ZnO (AZO) nanoparticles were spin-coated at 3500 rpm for 30 seconds, followed by an annealing at 110 °C for 20 minutes. An ITO layer was then sputtered using a Kenosistic (KS400) system. Finally, a MgF_2 anti-reflective coating was thermally evaporated.

$Cs_{0.17}FA_{0.83}Pb(I_{0.90}Br_{0.10})_3$ Device Fabrication

$Cs_{0.17}FA_{0.83}Pb(I_{0.90}Br_{0.10})_3$-based devices were fabricated following the architecture Glass or PET/ITO/MeO-2PACz/Perovskite/PEACl/C_{60}/AZO/ITO. We started from the procedure described in our previous work [55] using a dual-cation perovskite composition $Cs_{0.17}FA_{0.83}Pb(I_{0.9}Br_{0.1})_3$ at 1.45 M in a DMF:DMSO 4:1 solvent mixture. The precursor was doped with a triple-additive strategy including BMIM-BF_4, oleylamine (OAm), and benzylhydrazine hydrochloride (BHC), where BHC was added directly together with the perovskite precursors inside the glovebox at a concentration of 0.65 mg/mL. Stock solutions of BMIM-BF_4 and OAm were prepared in DMF at 50 µL/mL and stirred for 30 minutes; 20 µL of BMIM-BF_4 and 10 µL of

OAm stock were then added per 1 mL of perovskite solution. MeO-2PACz was deposited from a 0.33 mg/mL ethanol solution by spin coating at 5000 rpm for 30 s (5 s ramp). The perovskite solution was filtered (0.45 μm PTFE) and deposited by one-step antisolvent method: 80 μL of solution was spun at 6000 rpm for 35 s, with 150 μL of CB dropped after 20 s from a height of ~1–2 cm. Films were annealed at 105 °C for 20 min. A passivation layer of PEACl, 2 mg/mL in IPA, was spin-coated at 6000 rpm for 25 s and annealed at 100 °C for 5 min. C_{60} was thermally evaporated to a thickness of 28 nm. Finally, AZO nanoparticles (Avantama N-10) were spin-coated at 3500 rpm for 30 s and annealed at 110 °C for 20 min before deposition of ITO by RF magnetron sputtering.

Characterisation

Kesterite structural characterization was performed with a Rigaku Miniflex 600 in Bragg-Brentano geometry, with a Cu-Kα source (λ = 1.5446 Å) and a silicon array as the detector. Raman measurements were collected using a Renishaw's inVia Qontor microRaman microscope, with a 532 nm excitation wavelength, a nominal incident power of 1 mW, and a spot size of 0.25 μm. Current density-voltage (J-V) characteristics under 1 Sun illumination in Air Mass 1.5 G conditions were performed using a Keithley 6430 source meter in four-probe configuration and a LED-based G2V calibrated AAA solar simulator, with a light intensity of 87.8 mW/cm^2. The External Quantum Efficiency (EQE) spectra were collected using a Enlitech QE-R system calibrated with Si and Ge photodiodes, between 300 and 1400 nm. Scanning electron microscopy (SEM) images were taken using a Zeiss Series Auriga Field-emission microscope, with an acceleration voltage of 5 kV at a working distance ranging between 3 to 5 mm. Optical transmission and reflection measurements of SLG/ACZTSSe samples were recorded using a Jasco V-570 UV-visible spectrophotometer to determine the band gap by Tauc's plot [63].

Acknowledgments

The article is based upon work from COST Action Research and International Networking project "Emerging Inorganic Chalcogenides for PVs (RENEW-PV)," CA21148, supported by COST (European Cooperation in Science and Technology). E.S. is grateful to ICREA Academia program.

Funding

The authors thank Eni S.p.A. for funding C.G.'s PhD scholarship. The authors thank the research project "nuovi Concetti, mAteriali e tecnologie per l'iNtegrazione del fotoVoltAico negli edifici in uno scenario di generazione diffuSa" [CANVAS], funded by the Italian Ministry of the Environment and the Energy Security, through the Research Fund for the Italian Electrical System (type-A call, published on G.U.R.I. n. 192 on 18-08- 2022). This work was also supported by the "MUSA—Multilayered Urban Sustainability Action" project, funded by the European Union, via NextGenerationEU, under the National Recovery and Resilience Plan (NRRP) Mission 4 Component 2 Investment Line 1.5: Strengthening of research structures and creation of R&D "innovation ecosystems", set up of "territorial leaders in R&D". This project received funding from the European Union's H2020 ERC-Consolidator programme under grant agreement number no. 866018 (SENSATE), and by the Science and Innovation Ministry of Spain projects number PID2023-148976OB-C41 (CURIO-CITY) and PCI2023-145971-2 (ACT-FAST, CET-Partnership 2023 program). Y.G. thanks the European Union's Horizon research and innovation programme under the Marie Skłodowska-Curie grant agreement no. 10115148 (LEK-PV). The authors from UPC belong to the Micro and Nanotechnologies for Solar Energy Group (MNTSolar) Consolidated Research Group of the "Generalitat de Catalunya" (2021 SGR 01286). This work is also part of Maria de Maeztu Units of Excellence Programme CEX2023-001300-M / funded by MICIU/AEI /10.13039/501100011033. J.B. acknowledges the support of the Project "Network 4 Energy Sustainable Transition─NEST", Spoke 1, Project code PE0000021, funded under the National Recovery and Resilience Plan (NRRP), Mission 4, Component 2, Investment 1.3─Call for tender No. 1561 of 11.10.2022 of Ministero dell'Università e della Ricerca (MUR); funded by the European Union─NextGenerationEU. L.A.C. acknowledge the European Union's Framework Programme for Research and Innovation Horizon Europe (2021-2027) under the Marie Skłodowska-Curie Grant Agreement No. 101068387 "EFESO".

Author contributions

Carla Gobbo: Writing – original draft, Writing – review & editing, Visualisation, Validation, Methodology, Investigation, Data curation, Conceptualisation. Vanira Trifiletti: Writing – review & editing, Validation, Conceptualisation, Methodology. Giorgio Tseberlidis: Writing – review &

editing, Validation, Conceptualisation, Methodology. Yuancai Gong: Writing – review & editing, Methodology, Investigation, Formal analysis. Alex Jimenez-Arguijo: Writing – review & editing, Methodology, Investigation, Formal analysis. Chiara Boldrini: Investigation, Formal analysis. Jessica Barichello: Writing – review & editing, Methodology, Investigation, Formal analysis, Data curation, Validation. Luigi Angelo Castriotta: Writing – review & editing, Methodology, Investigation, Formal analysis, Data curation, Validation. Yassine Raoui: Methodology, Investigation, Formal analysis, Data curation. Paolo Mariani: Methodology, Investigation, Formal analysis. Fabio Matteocci: Methodology, Investigation, Formal analysis. Aldo Di Carlo: Writing – review & editing, Supervision, Resources, Funding acquisition. Paolo Biagini: Writing – review & editing, Supervision, Funding acquisition. Edgardo Saucedo: Writing – review & editing, Supervision, Resources, Funding acquisition. Riccardo Po: Writing – review & editing, Supervision, Resources, Funding acquisition. Simona Binetti: Writing – review & editing, Supervision, Resources, Project administration, Funding acquisition.

Competing interests

The authors declare no competing interests.

Data availability

The authors confirm that the data supporting the findings of this study are available within the article or its Supplementary Information.

References

1. Li, J. *et al.* Emergence of flexible kesterite solar cells: progress and perspectives. *npj Flexible Electronics* **7**, 16 (2023).
2. Huang, S. *et al.* A review on flexible solar cells. *Sci. China Mater.* **67**, 2717–2736 (2024).
3. Ramanujam, J. *et al.* Flexible CIGS, CdTe and a-Si:H based thin film solar cells: A review. *Prog. Mater. Sci.* **110**, 100619 (2020).
4. Lin, Q. *et al.* Flexible photovoltaic technologies. *J. Mater. Chem. C Mater.* **2**, 1233–1247 (2014).
5. He, M. *et al.* Kesterite Solar Cells: Insights into Current Strategies and Challenges. *Advanced Science* **8**, 2004313 (2021).
6. Green, M. A. *et al.* Solar Cell Efficiency Tables (Version 67). *Progress in Photovoltaics: Research and Applications* **n/a**, (2026).

7. Xu, X. *et al.* 12.84% Efficiency Flexible Kesterite Solar Cells by Heterojunction Interface Regulation. *Adv. Energy Mater.* **13**, 2301701 (2023).
8. Rehan, M. *et al. Flexible Monolithic 2-Terminal Kesterite Cu2ZnSnSe4 /Perovskite Tandem Solar Cells*. (2024). doi:10.21203/rs.3.rs-5405908/v1.
9. Jimenez-Arguijo, A. *et al.* Setting the baseline for the modelling of Kesterite solar cells: The case study of tandem application. *Solar Energy Materials and Solar Cells* **251**, 112109 (2023).
10. Ho-Baillie, A. W. Y. *et al.* Recent progress and future prospects of perovskite tandem solar cells. *Appl. Phys. Rev.* **8**, 041307 (2021).
11. Leijtens, T., Bush, K. A., Prasanna, R. & McGehee, M. D. Opportunities and challenges for tandem solar cells using metal halide perovskite semiconductors. *Nat. Energy* **3**, 828–838 (2018).
12. Wang, Z. *et al.* Regulation of Wide Bandgap Perovskite by Rubidium Thiocyanate for Efficient Silicon/Perovskite Tandem Solar Cells. *Advanced Materials* **36**, 2407681 (2024).
13. Luo, X. *et al.* Efficient Perovskite/Silicon Tandem Solar Cells on Industrially Compatible Textured Silicon. *Advanced Materials* **35**, 2207883 (2023).
14. Fu, F. *et al.* Monolithic Perovskite-Silicon Tandem Solar Cells: From the Lab to Fab? *Advanced Materials* **34**, 2106540 (2022).
15. Aydin, E. *et al.* Pathways toward commercial perovskite/silicon tandem photovoltaics. *Science (1979).* **383**, eadh3849 (2025).
16. Anaya, M., Lozano, G., Calvo, M. E. & Míguez, H. ABX3 Perovskites for Tandem Solar Cells. *Joule* **1**, 769–793 (2017).
17. Tang, L. *et al.* Record-Efficient Flexible Monolithic Perovskite–CIGS Tandem Solar Cell with VOC Exceeding 1.8 V on Polymer Substrate. *Adv. Energy Mater.* **15**, 2403682 (2025).
18. Fu, J. *et al.* A critical review of solution-process engineering for kesterite thin-film solar cells: current strategies and prospects. *J. Mater. Chem. A Mater.* **12**, 545–566 (2024).
19. Gong, Y. *et al.* Li-Doping and Ag-Alloying Interplay Shows the Pathway for Kesterite Solar Cells with Efficiency Over 14%. *Adv. Funct. Mater.* **34**, 2404669 (2024).
20. Colombo, B. E. G. *et al.* Above 10% efficiency flexible inkjet-printed kesterite solar cells. *Journal of Energy Chemistry* **117**, 880–892 (2026).
21. Wang, L. *et al.* Defects in kesterite materials towards high-efficiency solar cells: origin, impact, characterization, and engineering. *J. Mater. Chem. A Mater.* **12**, 25643–25677 (2024).
22. Wang, A., He, M., Green, M. A., Sun, K. & Hao, X. A Critical Review on the Progress of Kesterite Solar Cells: Current Strategies and Insights. *Adv. Energy Mater.* **13**, 2203046 (2023).
23. Zhou, J. *et al.* Control of the phase evolution of kesterite by tuning of the selenium partial pressure for solar cells with 13.8% certified efficiency. *Nat. Energy* **8**, 526–535 (2023).
24. Todorov, T., Gershon, T., Gunawan, O., Sturdevant, C. & Guha, S. Perovskite-kesterite monolithic tandem solar cells with high open-circuit voltage. *Appl. Phys. Lett.* **105**, 173902 (2014).
25. Li, Y. *et al.* Solution-processed perovskite-kesterite reflective tandem solar cells. *Solar Energy* **155**, 35–38 (2017).
26. Wang, D. *et al.* Interfacial Engineering of Wide-Bandgap Perovskites for Efficient Perovskite/CZTSSe Tandem Solar Cells. *Adv. Funct. Mater.* **32**, 2107359 (2022).

27. Rehan, M. *et al.* Defect Engineering in Earth-Abundant Cu2ZnSnSe4 Absorber Using Efficient Alkali Doping for Flexible and Tandem Solar Cell Applications. *ENERGY & ENVIRONMENTAL MATERIALS* **7**, e12604 (2024).
28. Hwang, S. K. *et al.* Cs-treatments in Kesterite Thin-Film Solar Cells for Efficient Perovskite Tandems. *Small* **20**, 2307175 (2024).
29. Hwang, S. K. *et al.* Electrochemically Deposited CZTSSe Thin Films for Monolithic Perovskite Tandem Solar Cells with Efficiencies Over 17%. *Energy & Environmental Materials* **7**, (2024).
30. Patil, J. V, Mali, S. S., Jang, J. S., Kim, J. H. & Hong, C. K. Approaching 24% Efficiency in Four-Terminal Perovskite/CZTSSe Tandem Solar Cells Using Diphenylammonium Chloride Additive-Based Wide-Bandgap Perovskite Absorber. *Small* **n/a**, 2501121 (2025).
31. Li, X. *et al.* Review and perspective of materials for flexible solar cells. *Materials Reports: Energy* **1**, 100001 (2021).
32. Jo, E. *et al.* 8% Efficiency Cu2ZnSn(S,Se)4 (CZTSSe) Thin Film Solar Cells on Flexible and Lightweight Molybdenum Foil Substrates. *ACS Appl. Mater. Interfaces* **11**, 23118–23124 (2019).
33. Dong, L., Cheng, S., Lai, Y., Zhang, H. & Jia, H. Sol-gel processed CZTS thin film solar cell on flexible molybdenum foil. *Thin Solid Films* **626**, 168–172 (2017).
34. Olgar, M. A., Erkan, S. & Zan, R. Comparative study of CZTS-based solar cells fabricated on Mo, Ni and Cu flexible substrates. *J. Alloys Compd.* **1011**, 178346 (2025).
35. Li, X. *et al.* Review and perspective of materials for flexible solar cells. *Materials Reports: Energy* **1**, 100001 (2021).
36. Park, H. K. *et al.* Flexible kesterite thin-film solar cells under stress. *npj Flexible Electronics* **6**, 91 (2022).
37. Park, H. K. *et al.* Chemical tailoring of sodium content for optimization of interfacial band bending and alignment in flexible kesterite solar cells. *Solar Energy Materials and Solar Cells* **230**, 111243 (2021).
38. Yang, K.-J. *et al.* Sodium Effects on the Diffusion, Phase, and Defect Characteristics of Kesterite Solar Cells and Flexible Cu2ZnSn(S,Se)4 with Greater than 11% Efficiency. *Adv. Funct. Mater.* **31**, 2102238 (2021).
39. Giraldo, S. *et al.* Progress and Perspectives of Thin Film Kesterite Photovoltaic Technology: A Critical Review. *Advanced Materials* **31**, 1806692 (2019).
40. Xu, H. *et al.* 9.63% efficient flexible Cu2ZnSn(S,Se)4 solar cells fabricated via scalable doctor-blading under ambient conditions. *J. Mater. Chem. A Mater.* **9**, 25062–25072 (2021).
41. Gong, Y. *et al.* Attaining 15.1% Efficiency in Cu2ZnSnS4 Solar Cells Under Indoor Conditions Through Sodium and Lithium Codoping. *Solar RRL* **9**, 2400756 (2025).
42. Kim, J. *et al.* Photo-excited carrier transport and secondary phases of Na-engineered kesterite flexible thin films. *Solar Energy Materials and Solar Cells* **250**, 112091 (2023).
43. López-Marino, S. *et al.* Alkali doping strategies for flexible and light-weight Cu2ZnSnSe4 solar cells. *J. Mater. Chem. A Mater.* **4**, 1895–1907 (2016).
44. Romanyuk, Y. E. *et al.* Doping and alloying of kesterites. *Journal of Physics: Energy* **1**, 044004 (2019).
45. Gong, Y. *et al.* Ag Incorporation with Controlled Grain Growth Enables 12.5% Efficient Kesterite Solar Cell with Open Circuit Voltage Reached 64.2% Shockley–Queisser Limit. *Adv. Funct. Mater.* **31**, 2101927 (2021).

46. Gershon, T. *et al.* Photovoltaic Materials and Devices Based on the Alloyed Kesterite Absorber (AgxCu1–x)2ZnSnSe4. *Adv. Energy Mater.* **6**, 1502468 (2016).
47. Yuan, Z.-K. *et al.* Engineering Solar Cell Absorbers by Exploring the Band Alignment and Defect Disparity: The Case of Cu- and Ag-Based Kesterite Compounds. *Adv. Funct. Mater.* **25**, 6733–6743 (2015).
48. Zaki, M. Y. & Velea, A. Recent Progress and Challenges in Controlling Secondary Phases in Kesterite CZT(S/Se) Thin Films: A Critical Review. *Energies (Basel).* **17**, 1600 (2024).
49. Dimitrievska, M. *et al.* Multiwavelength excitation Raman scattering of Cu2ZnSn(SxSe1−x)4 ($0 \le x \le 1$) polycrystalline thin films: Vibrational properties of sulfoselenide solid solutions. *Appl. Phys. Lett.* **105**, 031913 (2014).
50. Zhao, Q. *et al.* Effect of sodium doping on crystal growth and band matching of the heterojunction in flexible CZTS solar cells. *J. Mater. Chem. C Mater.* **9**, 17531–17541 (2021).
51. Engberg, S., Canulescu, S. & Schou, J. Liquid phase assisted grain growth in Cu2ZnSnS4 nanoparticle thin films by alkali element incorporation. *RSC Adv.* **8**, 7152–7158 (2018).
52. Braunger, D., Hariskos, D., Bilger, G., Rau, U. & Schock, H. W. Influence of sodium on the growth of polycrystalline Cu(In,Ga)Se2 thin films. *Thin Solid Films* **361–362**, 161–166 (2000).
53. Sangster, J. & Pelton, A. D. The Na-Se (Sodium-Selenium) System. *Journal of Phase Equilibria* **18**, 185–189 (1997).
54. Gobbo, C. *et al.* Strategies for Back Contact Engineering in High-Performance Flexible Kesterite Solar Cells. *J. Mater. Chem. A Mater.* https://doi.org/10.1039/D5TA03303A (2025) doi:10.1039/D5TA03303A.
55. Castriotta, L. A. *et al.* A universal multi-additive strategy to enhance efficiency and stability in inverted perovskite solar cells. *Nano Energy* **109**, 108268 (2023).
56. Raoui, Y. *et al.* Synergic MXene and S-benzyl-L-cysteine Passivation Strategies for Wide Bandgap Perovskite Solar Cells for 4T Tandem Applications. *Small* **21**, 2411310 (2025).
57. Larramona, G. *et al.* Stability, reliability, upscaling and possible technological applications of kesterite solar cells. *Journal of Physics: Energy* **2**, 024009 (2020).
58. Schutt, K. *et al.* Toward Fullerene-Free PIN Perovskite Solar Cells. *ACS Energy Lett.* **10**, 6307–6317 (2025).
59. Karimipour, M., Khazraei, S., Kim, B. J., Boschloo, G. & Johansson, E. M. J. Efficient and bending durable flexible perovskite solar cells via interface modification using a combination of thin MoS2 nanosheets and molecules binding to the perovskite. *Nano Energy* **95**, 107044 (2022).
60. Nawaz, M. H. *et al.* Flexible perovskite solar cells: advancements in materials, fabrication techniques, and future prospects. *Nano Converg.* **12**, 58 (2025).
61. Almalki, I. S. *et al.* Enhanced Efficiency and Mechanical Stability in Flexible Perovskite Solar Cells via Phenethylammonium Iodide Surface Passivation. *Nanomaterials* **15**, 1078 (2025).
62. Di Girolamo, D. *et al.* Breaking 1.7 V Open Circuit Voltage in Large Area Transparent Perovskite Solar Cells Using Interfaces Passivation. *Adv. Energy Mater.* **14**, 2400663 (2024).
63. Tauc, J., Grigorovici, R. & Vancu, A. Optical Properties and Electronic Structure of Amorphous Germanium. *physica status solidi (b)* **15**, 627–637 (1966).

Editorial summary:
Kesterites are promising bottom cells for efficient flexible perovskite tandems. Here, the authors report a solution-based route to fabricate high-efficiency kesterite bottom cells on rigid glass and flexible Mo substrates and design 4-terminal tandem devices combining kesterite and perovskite subcells.

Peer review information:
Communications Materials thanks William Jo and the other, anonymous, reviewer(s) for their contribution to the peer review of this work.

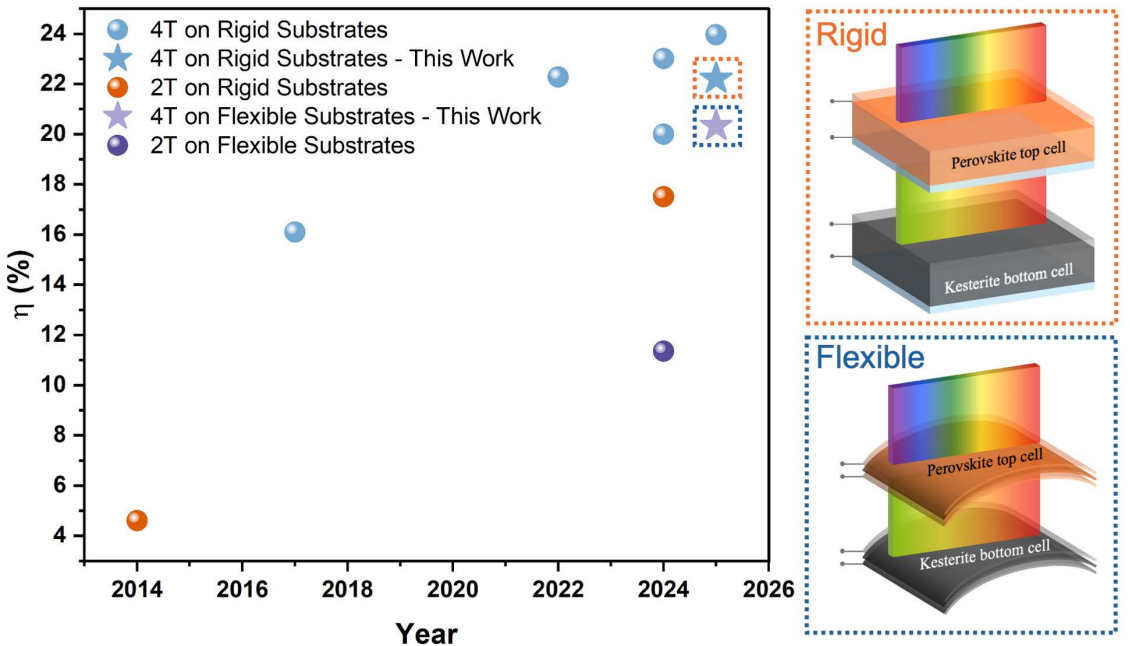
4T on Rigid Substrates
4T on Rigid Substrates - This Work
2T on Rigid Substrates
4T on Flexible Substrates - This Work
2T on Flexible Substrates
η (%)
Year
Rigid
Perovskite top cell
Kesterite bottom cell
Flexible
Perovskite top cell
Kesterite bottom cell